

Article

# Cobalt–Magnesium Oxide Catalysts for Deep Oxidation of Hydrocarbons

Magira Zhylykybek <sup>1,2</sup>, Bolatbek Khussain <sup>1</sup>, Alexandr Sass <sup>1</sup>, Ivan Torlopov <sup>1</sup>, Tolky Baizhumanova <sup>1,2</sup>, Svetlana Tungatarova <sup>1,2,\*</sup>, Alexandr Brodskiy <sup>1</sup>, Galina Xanthopoulou <sup>3</sup>, Kenzhegul Rakhmetova <sup>1</sup>, Rabiga Sarsenova <sup>1</sup>, Kaysar Kassymkan <sup>1</sup> and Yermek Aubakirov <sup>2</sup>

<sup>1</sup> D.V. Sokolsky Institute of Fuel, Catalysis and Electrochemistry, 142, Kunaev Str., Almaty 050010, Kazakhstan; magira.zhylykybek.90@mail.ru (M.Z.); b.khusain@ifce.kz (B.K.); aleksandr-sass@mail.ru (A.S.); myndfrea@gmail.com (I.T.); baizhuma@mail.ru (T.B.); albrod@list.ru (A.B.); rahmetova\_75@mail.ru (K.R.); rabinur@mail.ru (R.S.); kaysar\_007@mail.ru (K.K.)

<sup>2</sup> Department of Chemistry and Chemical Technology, Al-Farabi Kazakh National University, 71, Al-Farabi Str., Almaty 050040, Kazakhstan; miral.64@mail.ru

<sup>3</sup> Institute of Nanoscience and Nanotechnology, NCSR Demokritos, Aghia Paraskevi, 15310 Athens, Greece; g.xanthopoulou@inn.demokritos.gr

\* Correspondence: tungatarova58@mail.ru; Tel.: +7-727-291-6632 (S.T.)

**Abstract:** Co–Mg catalysts for methane combustion were synthesized and studied, revealing the transformation of MgCo<sub>2</sub>O<sub>4</sub> spinel into a CoO–MgO solid solution with oxygen release from the spinel lattice as the calcination temperature increased. Repeated heat treatment of the calcined solid solution at lower temperatures led to spinel regeneration with segregation of the solid solution phase. A TPR of the samples showed the presence of two characteristic peaks, the first of which relates to the transition of Co<sup>3+</sup><sub>OH</sub> spinel to the Co<sup>2+</sup><sub>OH</sub> structure of CoO, and the second to the reduction of CoO to Co<sup>0</sup>. The second peak was observed at 540–620 °C for samples calcined at temperatures below spinel decomposition, and for high-temperature samples at 900–1100 °C. Taking into account the identity of the structure of phases obtained in both cases, the formation of not a true CoO–MgO solid solution, but rather a mixture of ordered oxides (“pseudo-solid solution”) in the low-temperature region, was postulated. A study of the activity of the samples showed the high activity of the spinel systems and a linear relationship between the activation energy of methane oxidation and the heat treatment temperature.

**Keywords:** cobalt oxide; magnesium oxide; spinel; solid solution; deep oxidation of methane; oxidation catalyst



**Citation:** Zhylykybek, M.; Khussain, B.; Sass, A.; Torlopov, I.; Baizhumanova, T.; Tungatarova, S.; Brodskiy, A.; Xanthopoulou, G.; Rakhmetova, K.; Sarsenova, R.; et al.

Cobalt–Magnesium Oxide Catalysts for Deep Oxidation of Hydrocarbons.

*Catalysts* **2024**, *14*, 136. <https://doi.org/10.3390/catal14020136>

Academic Editor: Carlo Santoro

Received: 16 January 2024

Revised: 3 February 2024

Accepted: 5 February 2024

Published: 9 February 2024



**Copyright:** © 2024 by the authors. Licensee MDPI, Basel, Switzerland. This article is an open access article distributed under the terms and conditions of the Creative Commons Attribution (CC BY) license (<https://creativecommons.org/licenses/by/4.0/>).

## 1. Introduction

Methods based on the use of various catalytically active compositions are widely used in the purification of industrial gases from various organic products (methane and other hydrocarbons, carbon monoxide, soot, benzopyrene, aldehydes, etc.) [1–4]. Noble metals (Pt, Pd, Rh), as well as compositions based on metal oxides of variable valence, exhibit high activity in deep oxidation reactions. Among the oxides of 3d elements, cobalt oxide Co<sub>3</sub>O<sub>4</sub> and oxide systems based on it exhibit the highest activity in deep and partial oxidation reactions [4,5]. The high mobility of lattice oxygen in systems containing Co<sup>3+</sup> puts them on a par with catalysts based on noble metals in terms of specific activity [6]. The low cost of cobalt-oxide-based systems compared to scarce noble metals makes these catalysts especially promising [1–4].

The deep oxidation of methane and other hydrocarbons on oxide catalysts proceeds according to the Mars–van Krevelen mechanism [4,6], and therefore lattice oxygen plays a decisive role in their activity. This determines the importance of preserving the redox properties of catalysts along with their textural and mechanical characteristics, which is

ensured by depositing the cobalt-containing active component on an inert support. As a rule, a low-temperature alumina modification is used as the latter, with Co/Al<sub>2</sub>O<sub>3</sub> being the most common and well-studied Co-containing catalyst [4,7,8]. This system is characterized by deactivation under high-temperature conditions due to the formation of low-active CoAl<sub>2</sub>O<sub>4</sub> spinel and the fixation of active Co centers in the support lattice [7,8].

In order to provide increased thermal stability while maintaining the activity of the Co-catalyst, various structural promoters are usually introduced. Oxides of divalent cations (MgO, CaO, ZnO, etc.) are among such additives; they are capable of forming their own stable spinels with the alumina support [9,10]. The issue concerning the interaction of such promoters with the active component within binary systems of the CoO<sub>x</sub>-MeO type deserves special attention.

CoO<sub>x</sub>-MgO is one such promising system. It has been studied in the Fischer-Tropsch process [11], the dry reforming of methane [12,13], the steam reforming of organic compounds [14,15], and the partial [16,17] and, especially, the deep oxidation of methane [10,18–21]. The proximity of the radii of Co and Mg cations ensures the stability of the cubic structure of the oxide phases formed [22]. Two regions are present in the phase diagram of the Co-Mg oxide system: a low-temperature region, where MgCo<sub>2</sub>O<sub>4</sub> spinel is formed, and a high-temperature region of a continuous CoO-MgO solid solution. The phase transition between them occurs at 600–900 °C [23].

CoO-MgO high-temperature solid solutions have been considered in most work on the study of the structure, properties, and interactions between cations in this system [22]. A number of authors note the ability of a solid solution to stabilize Co<sup>2+</sup> ions in octahedral vacancies of the cubic structure, which are active in a number of catalytic processes such as the steam reforming of ethanol [14]. Other studies note the high thermal stability of CoO-MgO solid solutions and their low tendency to coking, which determines their high potential in the dry reforming of methane [12]. Recently, the number of studies on MgCo<sub>2</sub>O<sub>4</sub> spinel has increased in connection with the search for active components and supports for catalysts [24–27], as well as nanostructured compositions for electrocatalysis [28], thermochemical energy storage cycles [29], and electrodes for Li-ion batteries and supercapacitors [30,31]. However, studies examining the genesis of the Co-Mg oxide system during its heat treatment with the transition of the spinel into the solid solution are few and contradictory [12,31,32].

The deep oxidation of methane and other hydrocarbons occurs at high temperatures (550–800 °C) [1,4,6], with the temperature range of the catalyst operation partially coinciding with the region of phase transition, which determines the influence of mutual transformations between the spinel and the solid solution phases on the catalyst efficiency. Most importantly, reversible phase transitions of this type ensure the ability of the catalyst to regenerate after deactivation during thermal shocks or local overheating [12,27]. In this regard, establishing the patterns of formation of the CoO<sub>x</sub>-MgO oxide system as heat treatment proceeds and its effect on the catalytic activity using the example of the methane oxidation reaction is of particular relevance.

## 2. Results

### 2.1. Phase Composition and Structure of Samples

The structure of the synthesized catalyst samples with different heat treatment temperatures was studied by X-ray diffraction (XRD), Fourier-transform infrared spectroscopy (FTIR), scanning electron microscopy (SEM), and electron spin resonance (ESR) methods. The results of the X-ray phase analysis of the samples are presented in Figure 1. The obtained values of the positions of diffraction maxima and their correlation to phases are summarized in Table 1.

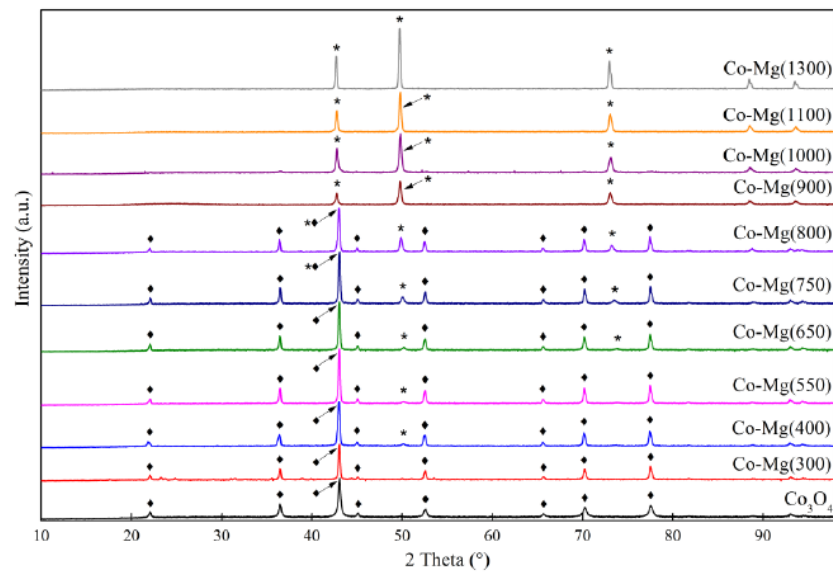


**Figure 1.** X-ray diffraction patterns of Co–Mg samples calcined in air at different temperatures, and  $\text{Co}_3\text{O}_4$  standard:  $\blacklozenge$ — $\text{MgCo}_2\text{O}_4$  (JCPDS 2–1073, JCPDS 81–671) or  $\text{Co}_3\text{O}_4$  (JCPDS 42–1467),  $*$ — $(\text{Co}, \text{Mg})\text{O}$  (JCPDS 45–946, JCPDS 48–1719).

**Table 1.** Diffraction maxima of XRD spectra and the corresponding phases of samples calcined at different temperatures.

Sample	Interplanar Distances (Å)	Lattice Parameter (Å)	Phase Composition
Co–Mg(300)	2.8593, 2.4436, 2.0213, 1.5559, 1.4291	8.086	$\text{MgCo}_2\text{O}_4$
Co–Mg(400)	2.8649, 2.4471, 2.0231, 1.5571, 1.4303 2.4471, 2.1118, 1.4912	8.095 4.223	$\text{MgCo}_2\text{O}_4$ $(\text{Co}, \text{Mg})\text{O}$ , $(\text{MgO})$
Co–Mg(550)	2.8598, 2.4438, 2.0219, 1.5564, 1.4296 2.4438, 2.1112, 1.4883	8.088 4.219	$\text{MgCo}_2\text{O}_4$ $(\text{Co}, \text{Mg})\text{O}$ , $(\text{MgO})$
Co–Mg(650)	2.8604, 2.4389, 2.0220, 1.5564, 1.4297 2.4389, 2.1094, 1.4963	8.089 4.219	$\text{MgCo}_2\text{O}_4$ $(\text{Co}, \text{Mg})\text{O}$
Co–Mg(750)	2.8588, 2.4378, 2.0209, 1.5558, 1.4291 2.4378, 2.1139, 1.4951	8.085 4.228	$\text{MgCo}_2\text{O}_4$ , $(\text{Co}, \text{Mg})\text{O}$
Co–Mg(800)	2.8630, 2.4408, 2.0232, 1.5568, 1.4299 2.4408, 2.1221, 1.5002	8.093 4.244	$\text{MgCo}_2\text{O}_4$ $(\text{Co}, \text{Mg})\text{O}$
Co–Mg(900)	2.8607, 2.4535, 2.0184, 1.5566, 1.4269 2.4535, 2.1247, 1.5020	8.086 4.249	$\text{MgCo}_2\text{O}_4$ $(\text{Co}, \text{Mg})\text{O}$
Co–Mg(1000)	2.4542, 2.1254, 1.5029	4.251	$(\text{Co}, \text{Mg})\text{O}$
Co–Mg(1100)	2.4543, 2.1256, 1.5028	4.251	$(\text{Co}, \text{Mg})\text{O}$
Co–Mg(1300)	2.4585, 2.1283, 1.5041	4.256	$(\text{Co}, \text{Mg})\text{O}$
Co–Mg(1100 + 750)	2.8625, 2.4466, 2.0284, 1.5614, 1.4363 2.4466, 2.1291, 1.5079	8.086 4.246	$\text{MgCo}_2\text{O}_4/\text{Co}_3\text{O}_4$ , $(\text{Co}, \text{Mg})\text{O}$
$\text{Co}_3\text{O}_4$	2.8585, 2.4375, 2.0209, 1.5557, 1.4290	8.084	$\text{Co}_3\text{O}_4$

Reflections characteristic of the spinel phase ( $\text{Co}_3\text{O}_4$ , JCPDS 42–1467 [27], or  $\text{MgCo}_2\text{O}_4$ , JCPDS 2–1073 [8,27,33], JCPDS 81–671 [34]) and the cubic oxide phases ( $\text{MgO}$ , JCPDS 45–946 [27], and  $\text{CoO}$ , JCPDS 48–1719 [24]) or their solid solution were observed in the diffraction patterns of the Co–Mg samples.

Cobalt oxide  $\text{Co}_3\text{O}_4$  is a standard normal spinel  $\text{A}^{2+}\text{B}_2^{3+}\text{O}_4$ , with tetrahedral vacancies occupied by  $\text{Co}^{2+}$  cations, and octahedral vacancies by  $\text{Co}^{3+}$  ( $\text{Co}^{2+}[\text{Co}^{3+}\text{O}_4]$ ) [35]. In

addition to normal spinels, inverse spinels  $B^{3+}[A^{2+}B^{3+}O_4]$  are known, in which divalent cations occupy an octahedral position, while half of the trivalent cations occupy a tetrahedral position [36], as well as intermediate spinels characterized by a certain degree of inversion. Calculations using the  $Co_3O_4-Al_2O_3$  system as an example [37] indicate a direct relationship between the degree of spinel inversion and its lattice parameter. The latter, according to the literature data for  $MgCo_2O_4$ , is characterized by a significant scatter (8.123 [33], 8.139 [34], 8.086 [38], 8.107 [39], 8.09 [40]). This suggests that the degree of inversion of the Co–Mg spinel is largely determined by the sample preparation technique. In this study, the spinel lattice parameter remained approximately constant with increasing heat treatment temperature (Table 1). The average lattice parameter was 8.089 Å, which supposedly corresponds to a low degree of spinel inversion. However, the large spread of the lattice parameter values prevents obtaining unambiguous results regarding the formation of a single phase of constant composition that would not depend on the heat treatment temperature. The absence of characteristic MgO reflections in the diffraction patterns of the samples indicates the formation of the  $Mg_xCo_{3-x}O_4$  compound under these conditions rather than a mixture of MgO and  $Co_3O_4$ , contrary to [23].

The gradual formation of a Co–Mg substitutional solid solution from the spinel phase was observed during heat treatment at temperatures above 550–650 °C. A further increase in temperature led to a sharp increase in the content of the solid solution and the complete disappearance of the spinel at ~1000 °C (Figure 2).

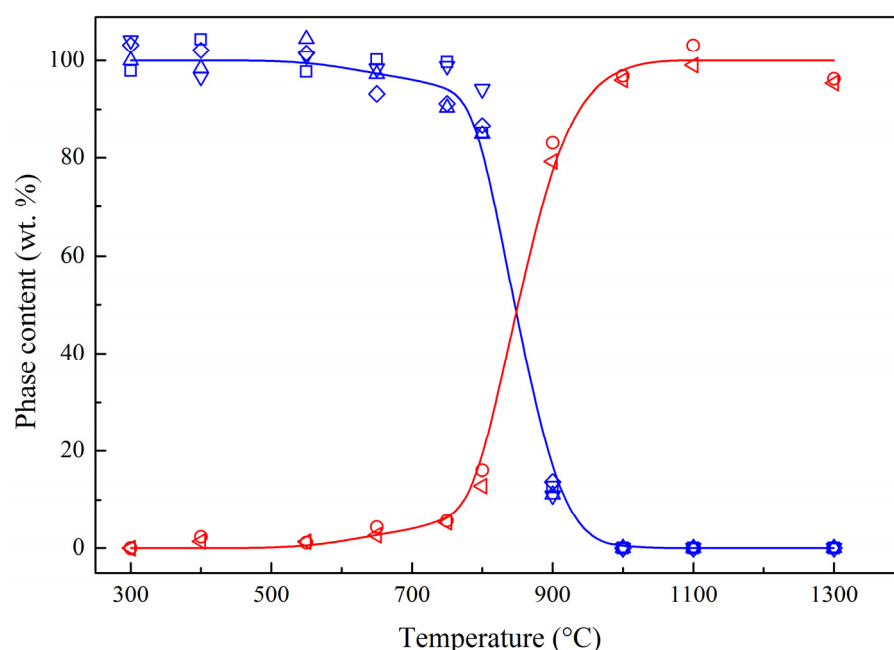


**Figure 2.** Influence of spinel heat treatment temperature on the content of spinel and solid solution phases according to X-ray diffraction data: — spinel phase:  $\nabla$ — $S_{2.86}/S_{2.44}$ ,  $\triangle$ — $S_{2.02}/S_{2.44}$ ,  $\square$ — $S_{1.56}/S_{2.44}$ ,  $\diamond$ — $S_{1.43}/S_{2.44}$ . — solid solution phase:  $\circ$ — $S_{2.12}/S_{2.44}$ ,  $\triangleleft$ — $S_{1.50}/S_{2.44}$ .

At low calcination temperatures, the cubic oxide phase was characterized by lattice parameter values close to the values for pure MgO (Table 1) [12,32]. The lattice parameter increased and reached a value approximately corresponding to the Mg:Co = 1:2 ratio [41], indicating the formation of the solid solution phase.

This is explained by the presence of residual MgO at low temperatures. A sharp increase in the lattice parameter of the solid solution occurs simultaneously with the accumulation of this phase during heat treatment and corresponds to the saturation of the solid solution with cobalt.

The X-ray phase analysis of the Co–Mg(1100 + 750) sample subjected to secondary heat treatment, compared with the initial Co–Mg(1100) sample, showed the presence of a

spinel phase along with the solid solution formed at 1100 °C (Table 1). This confirms the possibility of the reoxidation of a part of the  $\text{Co}^{2+}$  in the solid solution structure into  $\text{Co}^{3+}$  in an oxygen-containing atmosphere with the spinel phase formation [23]. From X-ray diffraction data, it is impossible to determine which formula the resulting spinel phase corresponds to:  $\text{Co}_3\text{O}_4$  or  $\text{MgCo}_2\text{O}_4$ .

The results of the FTIR study of the structure of the synthesized samples are presented in Figure 3.

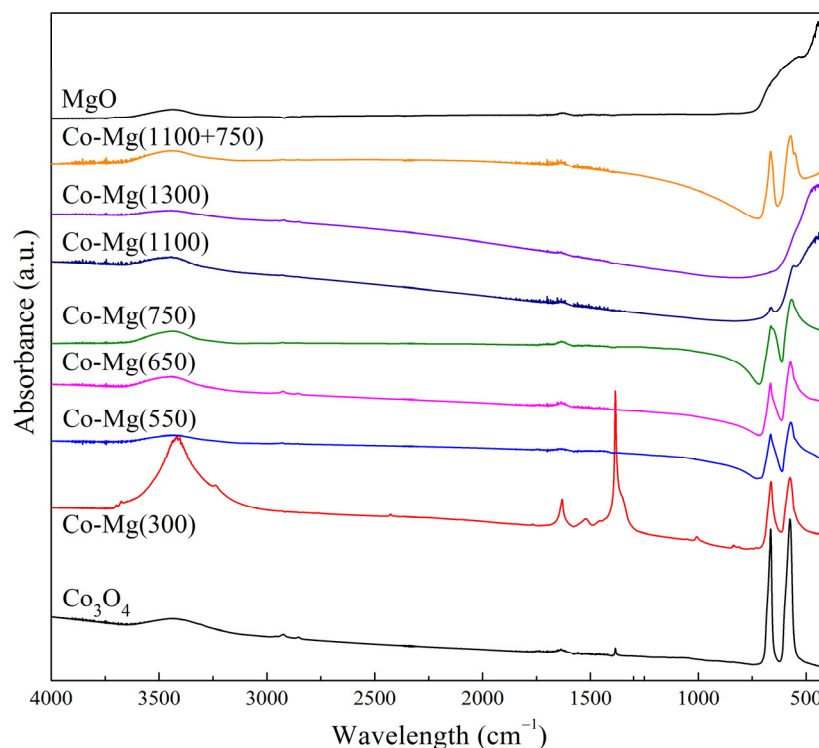


**Figure 3.** FTIR spectra of Co–Mg samples calcined at various temperatures and standard  $\text{Co}_3\text{O}_4$  and MgO.

Absorption bands (a.b.) characteristic of  $\nu\text{H}_2\text{O}$  vibrations ( $3420\text{--}3450$ ,  $1630\text{--}1640\text{ cm}^{-1}$ ) are present in the spectra of all samples. Residual  $\text{NO}_3^-$  ( $3700$ ,  $1630$ ,  $1520$ ,  $1390\text{ cm}^{-1}$ ) and OH-groups ( $3420\text{--}3450\text{ cm}^{-1}$ ) are present in the Co–Mg(300) sample. The key feature of the spectra is the region of  $700\text{--}400\text{ cm}^{-1}$ , where for samples calcined at temperatures below  $1100\text{ °C}$ , two a.b. are observed ( $660\text{--}670$  and  $560\text{--}575\text{ cm}^{-1}$ ), corresponding to the  $\nu_1$  and  $\nu_2$  stretching vibrations of Me–O [40]. Their positions are consistent with the a.b. of  $\text{Co}_3\text{O}_4$  ( $575$  and  $664\text{ cm}^{-1}$ ) [42,43] and are characterized by a slight shift depending on the heat treatment temperature (Figure 4).

A further increase in calcination temperature leads to the almost complete disappearance of the  $\nu_1$  and  $\nu_2$  absorption bands and the appearance of an intense broad band with a.b. at  $440\text{--}445\text{ cm}^{-1}$ , which correlates with similar a.b. of MgO ( $440\text{ cm}^{-1}$ ) [21]. In the case of the Co–Mg(1100 + 750) sample subjected to reoxidation,  $\nu_1$  and  $\nu_2$  a.b. characteristic of spinel are observed, with  $\nu_1$  split into a.b. at  $551$  and  $571\text{ cm}^{-1}$ .

The bands at  $660\text{--}670$  and  $560\text{--}575\text{ cm}^{-1}$  are attributed to the stretching vibrations of the Me–O bonds of the spinel structure. The  $\nu_1$  band is associated with vibrations of bonds between cations located in octahedral vacancies ( $\text{O-B}_3$ ), and  $\nu_2$  with vibrations of bonds between cations in both tetrahedral and octahedral voids ( $\text{A-B-O}_3$ ) [42,43]. Thus, the shift of the  $\nu_1$  band to the lower region indicates an increase in the length of the bonds of cations in octahedral positions.

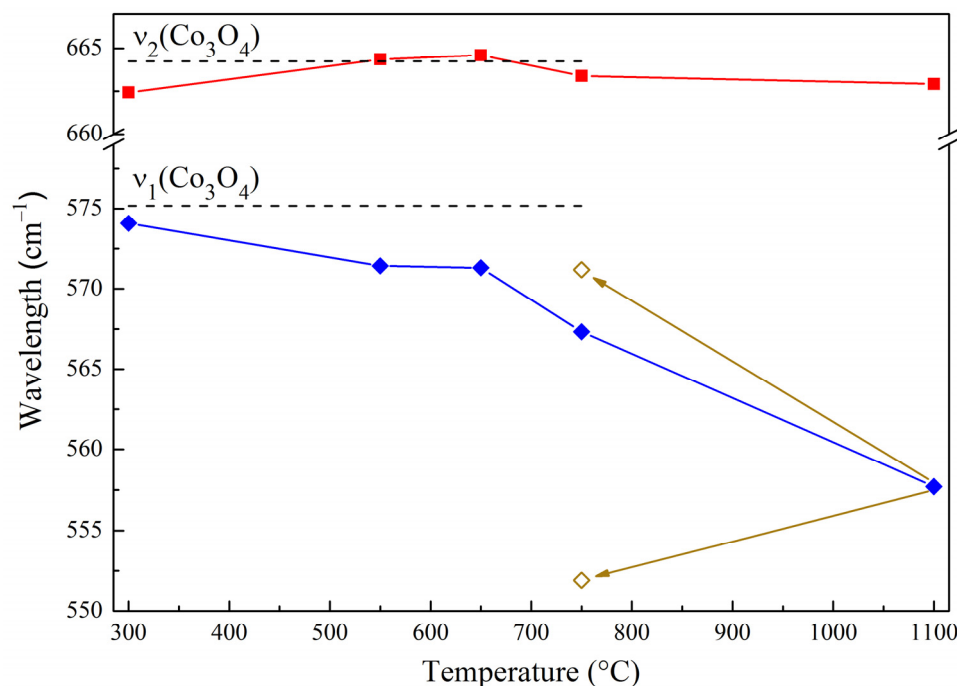


**Figure 4.** Dependence of the position of a.b. on the FTIR spectra of samples on the heat treatment temperature: — $\nu_1$  a.b., — $\nu_2$  a.b., —changes in the position of bands during reoxidation.

The shift in  $\nu_1$  is especially strong at heat treatment temperatures above 650 °C, when, according to the X-ray diffraction data, the spinel structure decomposes and the solid solution forms. This is explained by the partial reoxidation of the surface of the solid solution during rapid cooling in air after heat treatment. The crystal lattice of the solid solution phase causes distortions in the spinel phase formed on its surface during reoxidation. Longer/deeper reoxidation leads to the further growth of the spinel phase and, at the same time, its partial restructuring into an undistorted structure (healing of defects), which explains the preservation of the a.b. at 551 cm<sup>-1</sup> in the form of a shoulder with the main band at 571 cm<sup>-1</sup>.

To further study the state of Co cations, the ESR method was used. Theoretically, Co<sup>3+</sup><sub>Oh</sub> species of the bulk MgCo<sub>2</sub>O<sub>4</sub> structure are diamagnetic and lack an ESR signal. In the solid solution, Co<sup>2+</sup> ions occupy octahedral vacancies and give a signal with  $g = 4.23\text{--}4.28$  at temperatures lower than  $-153$  °C that disappears at higher temperatures due to the Jahn–Teller effect [44–46]. However, the ESR spectra of the synthesized samples showcase a broad isotropic singlet with  $g = 2.25$ , related to the Co<sup>2+</sup> species in a tetrahedral environment with the 3d<sup>5</sup> electronic configuration [43,47] (Table 2, Figure 5).

**Table 2.** Relative ESR signal of samples depending on heat treatment temperature.

Sample	Ratio of Signal and Standard Intensities
Co–Mg(300)	0.50
Co–Mg(400)	1.35
Co–Mg(550)	1.46
Co–Mg(650)	1.51
Co–Mg(750)	1.56
Co–Mg(800)	0.88
Co–Mg(900)	0.58
Co–Mg(1000)	0.49
Co–Mg(1100)	0.51
Co–Mg(1300)	0.24
Co <sub>3</sub> O <sub>4</sub>	6.63

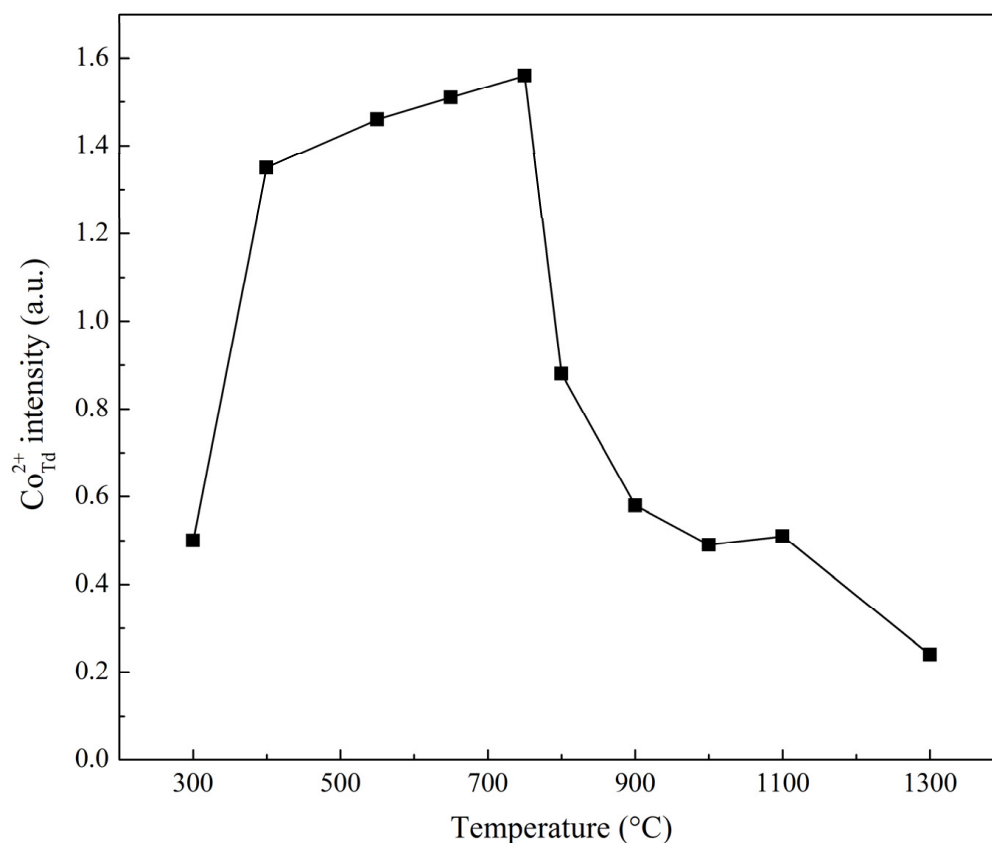


**Figure 5.** Influence of the heat treatment temperature of Co–Mg samples on the relative intensity of the ESR signal of  $\text{Co}^{2+}_{\text{Td}}$  ions.

The appearance of  $\text{Co}^{2+}_{\text{Td}}$  cations is possible only in the case of  $\text{Co}_3\text{O}_4$  spinel. Such a spinel could theoretically be formed along with  $\text{MgCo}_2\text{O}_4$  following cobalt and magnesium nitrate decomposition during the synthesis of samples. According to Table 2, a certain amount of  $\text{Co}^{2+}_{\text{Td}}$ , i.e.,  $\text{Co}_3\text{O}_4$ , is present in the synthesized samples up to the temperature range of the spinel phase decomposition (up to 750 °C). The amount of  $\text{Co}^{2+}_{\text{Td}}$  sharply decreases in parallel with the decrease in the amount of spinel with a further increase in the calcination temperature (Figure 2). Small residual amounts of  $\text{Co}^{2+}_{\text{Td}}$  in high-temperature samples are apparently associated with the partial reoxidation of the CoO–MgO solid solution during the rapid cooling of the samples after heat treatment, which can have a dramatic effect on the surface phase composition: in this regard, in works [22,32] dealing with solid solutions, inert, oxygen-free media were used to eliminate spinel formation.

The morphology of particles and the elemental composition of a number of synthesized samples were studied by scanning electron microscopy. Typical micrographs of spinel and solid solution are shown in Figure 6.

According to SEM data, the spinel phase (Figure 6a,b) is formed by irregular, weakly crystallized plate-type particles 0.5–2.5  $\mu\text{m}$  in size and secondary aggregates up to 10  $\mu\text{m}$  in size. The Co–Mg solid solution phase formed during high-temperature calcination showcases octahedral crystals with sizes of 1–3  $\mu\text{m}$ , which are also prone to aggregation. This is consistent with the data on the cubic structure of the solid solution, which is prone to the formation of octahedral particles [22].

Table 3 shows the results of the analysis of the elemental composition of the samples.

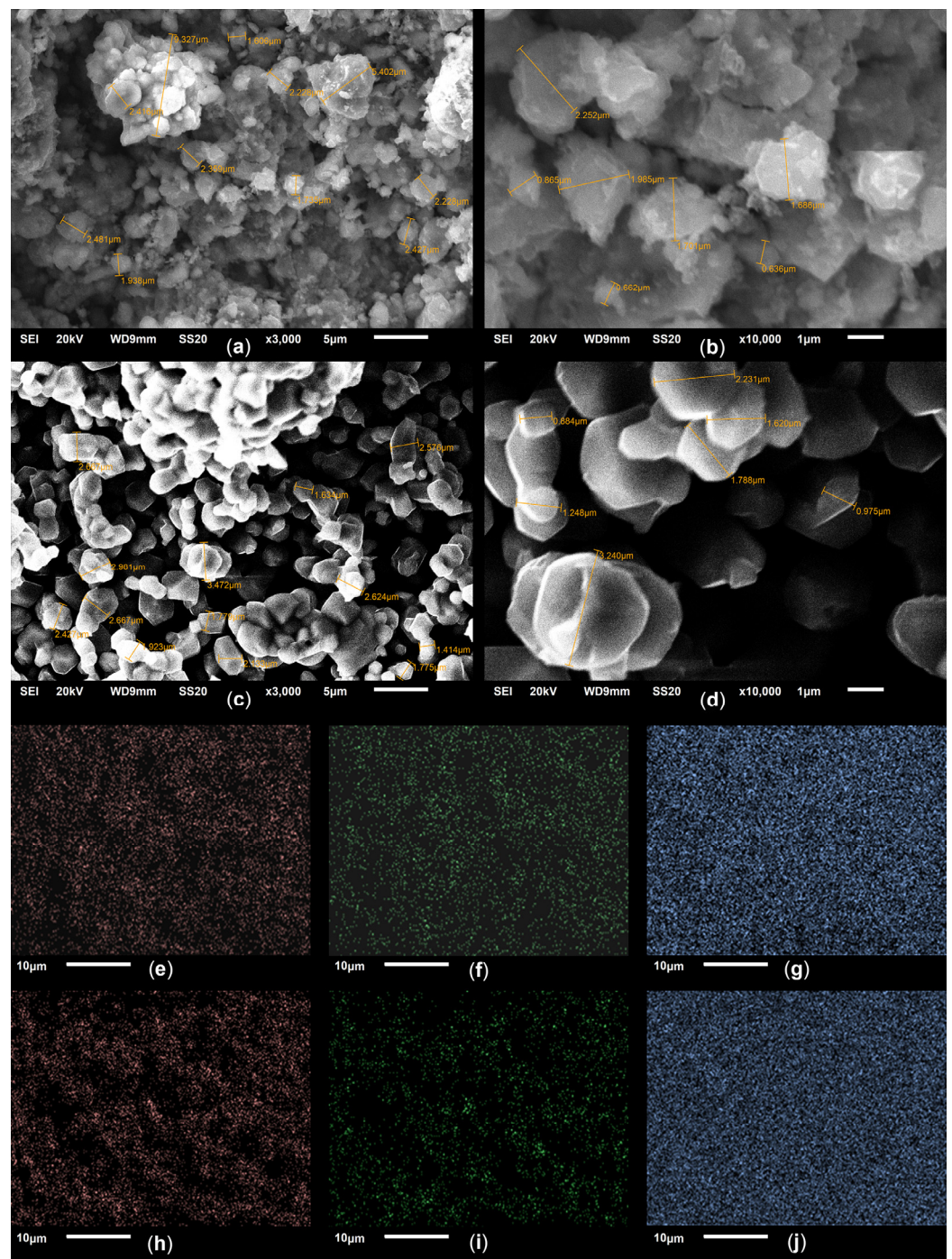


**Figure 6.** SEM micrographs: (a,b)—Co-Mg(400) sample; (c,d)—Co-Mg(1100) sample; (a,c)—magnification 3000; (b,d)—magnification 10,000; EDX analysis images: (e–g)—Co-Mg(1100) sample; (h–j)—Co-Mg(1100 + 750) sample; (e,h)—O K; (f,i)—Mg K; (g,j)—Co K.

A study of the elemental composition of the samples showed a monotonous increase in the Co:Mg ratio in the surface layers with increasing heat treatment temperature. The lack of Co relative to the stoichiometric ratio for spinel 2:1 in the case of Co-Mg(400) can be explained by the suggestion that incompletely decomposed magnesium nitrate formed a film on the surface of the sample grains during synthesis at this temperature [48]. A further increase in the calcination temperature to 750 °C gives Co:Mg values close to stoichiometry. The excess of Co in the case of the Co-Mg(1100) sample, which comprises a CoO-MgO solid solution, is probably explained by the partial migration of Mg into the bulk phase

during the formation of a  $\text{Co}_3\text{O}_4$  spinel phase on the surface during the rapid cooling of the sample. The formation of  $\text{Co}_3\text{O}_4$  under these conditions is confirmed by FTIR spectroscopy data (Figure 3).

**Table 3.** Local elemental composition of Co–Mg samples.

Sample	Point of Analysis	Amount of Element per Unit Mg			Sum of Elements
		O	Mg	Co	
Co–Mg(400)	Point 1	1.54	1.00	1.24	3.78
	Point 2	1.78	1.00	1.28	4.06
	Point 3	1.64	1.00	1.32	3.96
	Average	1.64	1.00	1.28	3.92
Co–Mg(750)	Point 1	1.85	1.00	1.61	4.46
	Point 2	1.90	1.00	1.81	4.71
	Point 3	1.91	1.00	1.64	4.55
	Average	1.89	1.00	1.69	4.58
Co–Mg(1100)	Point 1	3.03	1.00	3.35	7.38
	Point 2	2.95	1.00	3.13	7.08
	Point 3	3.05	1.00	3.24	7.29
	Average	3.00	1.00	3.24	7.24
Co–Mg(1100 + 750)	Point 1	3.30	1.00	6.09	10.39
	Point 2	3.14	1.00	4.59	8.73
	Point 3	1.83	1.00	2.30	5.13
	Average	2.51	1.00	3.77	7.28

The reoxidation of the solid solution leads to a significant increase in the spread of the Co:Mg ratio at different survey points. This, apparently, is caused by the phase segregation of the solid solution due to the uneven formation of the bulk spinel phase, enriched in cobalt compared to the solid solution.

The amount of oxygen in all samples was lower than stoichiometric for any of the possible compounds in the system of this composition (Co:Mg = 2:1), which is explained by the partial reduction in cobalt in the samples under the action of an electron beam during analysis (such an effect was not observed for pure MgO). At the same time, the initially oxidized samples showcase the small spread of oxygen content at different local points, confirming their homogeneity. Significant fluctuations in the amount of oxygen at different survey points were observed in the case of the Co–Mg(1100 + 750) sample, further confirming the formation of a cobalt-enriched spinel phase, which decomposes more easily. This effect is further substantiated by EDX analysis data (Figure 6).

## 2.2. Binding Energy and Oxygen Reactivity of Samples

Oxygen associated with the surface and structure of the catalyst is important in catalytic deep oxidation reactions [4,6]. Lattice oxygen, the amount of which determines the catalyst specific activity, plays a particularly important role in the reaction of methane deep oxidation, which occurs at temperatures of 550–800 °C according to the Mars–van Krevelen mechanism [6]. In this regard, temperature-programmed desorption of oxygen (TPD) and temperature-programmed reduction by hydrogen ( $\text{H}_2$ -TPR) methods were used to study the amount of different types of oxygen.

The results of the study of the catalyst samples using TPD analysis are presented in Figure 7. Table 4 shows the quantitative characteristics of the thermal desorption of the samples: temperatures of oxygen release maxima, volumes of oxygen released during desorption, and desorption activation energies for different regions.

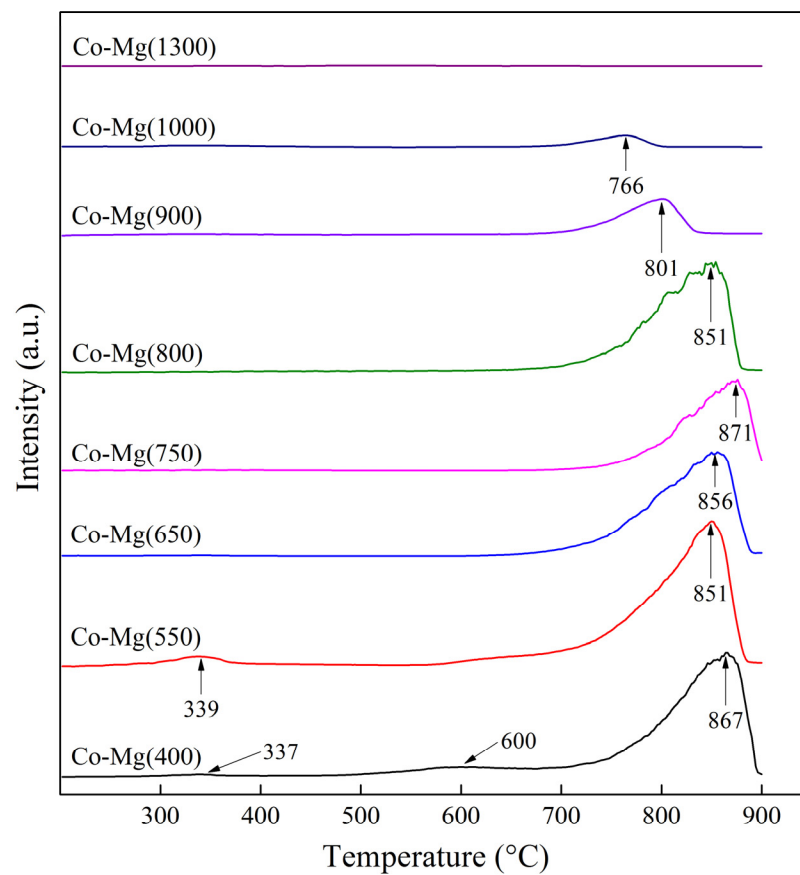


**Figure 7.** Thermal desorption profiles of synthesized samples for different calcination temperatures.

**Table 4.** Characteristics of thermal desorption of synthesized samples for different calcination temperatures.

Sample	Desorption Peak Temperatures (°C)			Volume of O <sub>2</sub> Release in the Temperature Range (mL/g)		Activation Energies (kJ/mol)		
	1	2	3			1	2	3
Co-Mg(400)	337	600	867	14.32 (200–450)	652.50 (500–900)	49.1	80.6	168.0
Co-Mg(550)	339	651	851	58.60 (200–450)	719.92 (550–900)	44.0	116.1	142.3
Co-Mg(650)	335	-	856	8.02 (200–450)	516.79 (600–900)	9.5	-	192.0
Co-Mg(750)	343	-	871	8.22 (200–450)	459.03 (600–900)	11.0	-	212.5
Co-Mg(800)	-	-	851	11.43 (200–450)	500.64 (600–900)	17.5	-	203.8
Co-Mg(900)	328	-	801	18.44 (200–450)	150.99 (600–900)	18.8	-	201.3
Co-Mg(1000)	335	-	766	12.8 (200–450)	38.46 (600–900)	25.2	-	232.3
Co-Mg(1300)	365	-	695	2.40 (200–450)	6.20 (500–900)	10.4	-	213.9

Oxygen desorption occurs in three regions (Figure 7): 1—300–400 °C, 2—600–650 °C, and 3—650–900 °C, with characteristic maxima (Table 4). There is a peak in region 2 on the Co–Mg(400) sample, which turns into a shoulder upon transition to Co–Mg(550) and disappears with a further increase in the heat treatment temperature. The oxygen released during thermal desorption was divided into two parts: low temperature (region 1, characterized by the desorption of physically adsorbed oxygen) and high temperature (regions 2 and 3, associated with the stepwise desorption of lattice oxygen).

Region 1 is characterized by relatively high desorption activation energies (45–50 kJ/mol) at low heat treatment temperatures (400–550 °C). This can be explained by the fact that these samples contain the products of incomplete decomposition of the initial cobalt and magnesium nitrates. A further increase in the calcination temperature leads to a decrease in the activation energy of desorption of region 1 to 10–25 kJ/mol, which is a typical value for physically adsorbed oxygen [22].

Regions 2 and 3 are characterized by a much more intense release of oxygen due to the decomposition of Co–Mg compounds. Stepwise decomposition is observed, presumably due to the incomplete formation of the spinel crystal lattice in the case of low-temperature samples (400–550 °C). The activation energies of desorption under these conditions are 80–120 and 140–170 kJ/mol for the first and second stages, respectively. Regions 2 and 3 merge into one with a further increase in the calcination temperature. The activation energy remains approximately constant (190–210 kJ/mol) at temperatures of 650–1300 °C. The total amount of released oxygen monotonously decreases in this heat treatment temperature range. A particularly sharp drop is observed at temperatures above 800 °C, which corresponds to the formation of a solid solution phase.

Reflections characteristic of the CoO–MgO solid solution were present in the diffraction pattern of the Co–Mg(650) sample subjected to thermal desorption up to 900 °C (Figure 8). Thus, oxygen desorbed in the high-temperature region is supposedly associated with the decomposition of  $\text{MgCo}_2\text{O}_4$  spinel and its transition into a solid solution, which is substantiated by [22,49,50], where oxygen release from different cobalt oxide structures was observed.

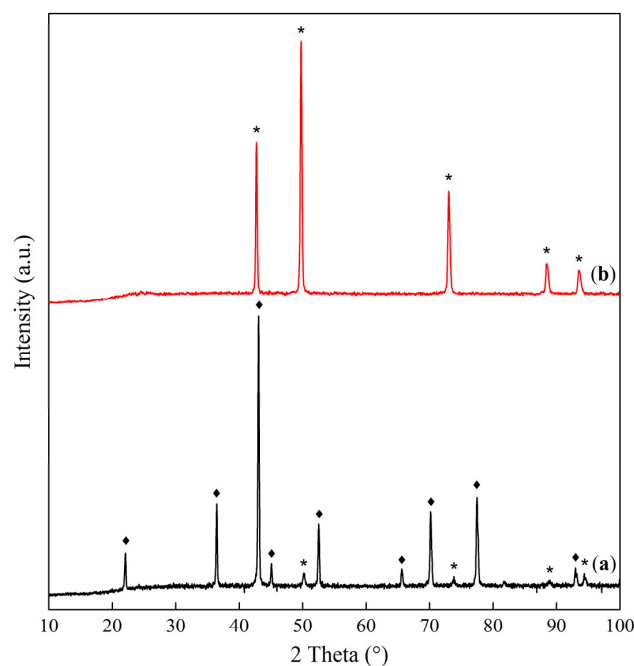


**Figure 8.** Diffraction patterns of a sample calcined at 650 °C before (a) and after (b) TPD up to 900 °C:  $\blacklozenge$ — $\text{MgCo}_2\text{O}_4$  (JCPDS 2–1073, JCPDS 81–671) or  $\text{Co}_3\text{O}_4$  (JCPDS 42–1467), \*—(Co, Mg)O (JCPDS 45–946, JCPDS 48–1719).

Figure 9 shows the TPR profiles of the synthesized samples for different heat treatment temperatures in comparison with  $\text{Co}_3\text{O}_4$ . Table 5 summarizes the quantitative characteristics of the TPR profiles of the samples.

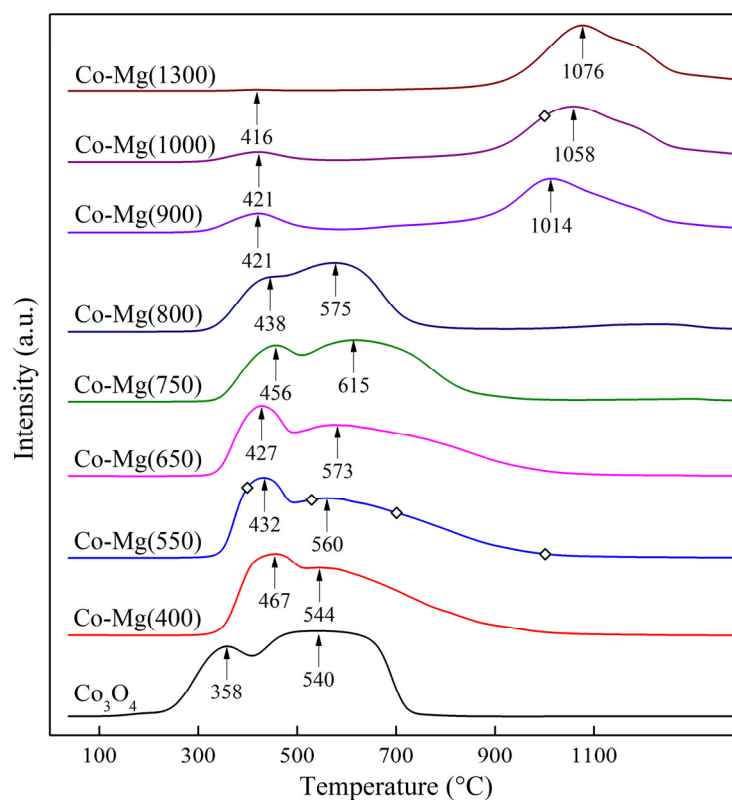


**Figure 9.** TPR profiles of synthesized samples for different heat treatment temperatures: ◊—TPR stopping points.

**Table 5.** Amount of hydrogen consumed corresponding to the TPR peaks of samples calcined in air and its total amount in mmol/g.

Temperature (°C)	Peak 1	Peak 2	Total Peak Area	Peak Area Ratio
$\text{Co}_3\text{O}_4$	4.51	13.10	17.61	1:2.90
Co-Mg(400)	5.53	9.34	14.71	1:1.69
Co-Mg(550)	4.81	10.04	14.86	1:2.09
Co-Mg(650)	4.20	10.25	14.48	1:2.44
Co-Mg(750)	3.57	9.74	13.32	1:2.73
Co-Mg(800)	2.82	9.48	12.29	1:3.36
Co-Mg(900)	1.49	9.71	11.19	1:6.52
Co-Mg(1000)	1.03	9.90	10.93	1:9.61
Co-Mg(1300)	0.07	9.76	9.83	–

It is known from the literature that the reduction in  $\text{Co}_3\text{O}_4$  occurs in two temperature regions: in the first region,  $\text{Co}^{3+}$  is reduced to  $\text{Co}^{2+}$ , and in the second,  $\text{Co}^{2+}$  is reduced to  $\text{Co}^0$  [9,25–27,42]. The stoichiometric ratio of oxygen in the first and second regions is 1:3. This agrees well with the data in Table 5. When replacing Co in this spinel with Mg, the theoretical ratio between them should change to 1:2. This ratio is approximately maintained at heat treatment temperatures of 400–650 °C, after which it increases due to a decrease in the amount of  $\text{Co}^{3+}$  in the samples as the spinel phase transitions to a solid solution. At the same time, starting from these temperatures (750 °C and above), a gradual decrease in the total amount of oxygen capable of reduction is observed (Table 5). All samples at the end of TPR consisted of  $\text{Co}^0$  and MgO phases.

The TPR profiles of the samples calcined in the temperature range 400–800 °C are similar to those commonly presented in the literature [9,12,16,25–27]. The first reduction peak is observed at 420–470 °C, and the second, much broader, stretches to ~900 °C and is characterized by a maximum at 540–620 °C. A further increase in heat treatment temperature with the transition of spinel into a solid solution led to a gradual transformation of the TPR profiles. The first peak (410–420 °C) decreased significantly, while the second peak underwent a significant shift to the high-temperature region (maximum at 1010–1080 °C). These TPR profiles are partially described in the works of Wang and Ruckenstein [12,16], in which an increase in hydrogen consumption is observed before the stop of their TPR experiments at 1000 °C, with the maximum intake not reached.

A series of experiments involving stopping the TPR process at certain temperatures was carried out to study, in detail, the change in phase composition during the reduction of the samples. Temperatures of 400, 530, 700, and 1000 °C were chosen for the Co–Mg(550) sample, and 1000 and 1100 °C—for the Co–Mg(1000) sample (Figure 9). The results of the analysis of the phase composition of the resulting reduced samples are presented in Figures 10–12.

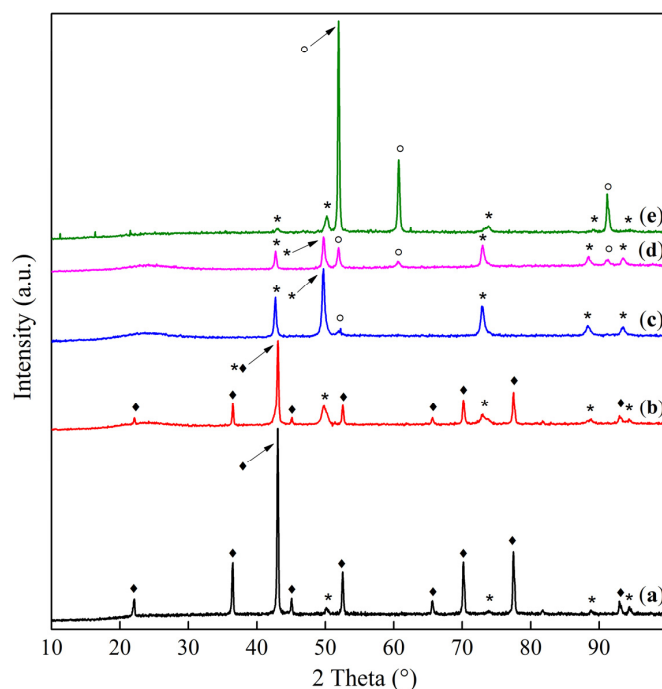


**Figure 10.** Diffraction patterns of a sample calcined at 550 °C before (a) and after TPR: (b) up to 400 °C, (c) up to 530 °C, (d) up to 700 °C and (e) up to 1000 °C:  $\blacklozenge$ — $\text{MgCo}_2\text{O}_4$  (JCPDS 2–1073, JCPDS 81–671) or  $\text{Co}_3\text{O}_4$  (JCPDS 42–1467),  $*$ — $(\text{Co}, \text{Mg})\text{O}$  (JCPDS 45–946, JCPDS 48–1719),  $\circ$ — $\beta\text{-Co}^0$  (JCPDS 15–806).

According to the X-ray diffraction data, peaks from the solid solution phase appear in its diffraction pattern when the Co–Mg(550) sample is reduced to 400 °C (in the region of the maximum of the first TPR peak), while the intensity of the spinel phase peaks decreases by half. A decrease in the intensity of the bands corresponding to the spinel phase is observed in the FTIR spectrum. An increase in the reduction temperature to 530 °C (the region between the first and second TPR peaks) leads to the complete disappearance of spinel peaks in the diffraction pattern and an increase in reflections from the CoO–MgO solid solution. The FTIR spectrum similarly demonstrates the disappearance of spinel a.b. and the appearance of a broad band of the solid solution ( $442\text{ cm}^{-1}$ ). A further increase in the final reduction temperature to 700 °C (the region of the maximum of the second TPR peak) causes the appearance of peaks of the metallic  $\text{Co}^0$  phase in the cubic  $\beta$ -form (JCPDS 15–806 [17]) in the diffraction pattern and a decrease in the intensity of reflections of the solid solution. Only the CoO–MgO a.b. ( $450\text{ cm}^{-1}$ ) is present in the FTIR spectrum, since metal phases are not observed by FTIR spectroscopy. The metallic  $\beta$ -cobalt and the

cubic oxide phase, which, in terms of the lattice parameter value, is rather the MgO phase than the CoO–MgO solid solution, are observed at a reduction temperature of 1000 °C, according to the X-ray diffraction data, while the FTIR spectrum showcases an a.b. with a maximum at 447  $\text{cm}^{-1}$ , again corresponding to the solid solution or MgO phase.

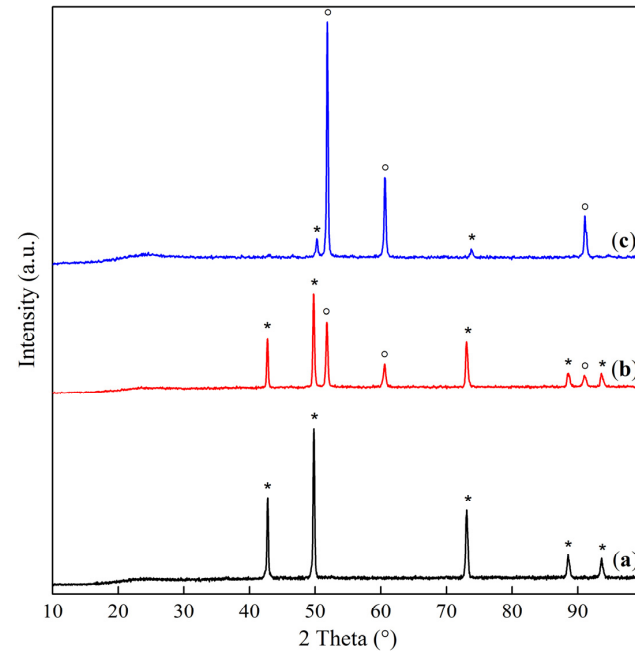


**Figure 11.** Diffraction patterns of a sample calcined at 1000 °C before (a) and after TPR: (b) up to 1000 °C and (c) up to 1100 °C: \*—(Co, Mg)O (JCPDS 45–946, JCPDS 48–1719), ○— $\beta$ -Co<sup>0</sup> (JCPDS 15–806).

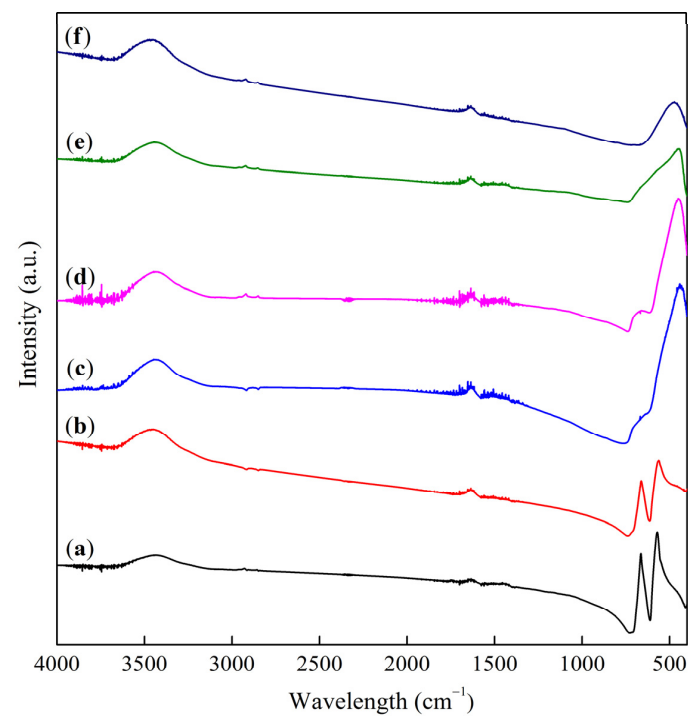


**Figure 12.** FTIR spectra of a sample calcined at 550 °C before (a) and after TPR: (b) up to 400 °C, (c) up to 530 °C, (d) up to 700 °C and (e) up to 1000 °C, as well as (f) sample calcined at 1000 °C after TPR up to 1000 °C.

The Co–Mg(1000) sample, which, according to the X-ray diffraction data, is a solid solution, after TPR up to 1000 °C is characterized by reflections of the solid solution and metallic cobalt phases. The overall peak intensity was lower than that of the original sample. FTIR spectroscopy data confirm the presence of a solid solution ( $473\text{ cm}^{-1}$ ). Reduction to 1100 °C gives reflections of  $\text{Co}^0$  and the MgO phase according to XRD.

Summarizing the obtained data, it can be argued that the first TPR peak relates to the absorption of oxygen in the spinel structure associated with  $\text{Co}^{3+}_{\text{Oh}}$  ions, with the reduction of  $\text{Co}^{3+}_{\text{Oh}}$  into the  $\text{Co}^{2+}_{\text{Oh}}$  structure of CoO, regardless of the heat treatment temperature of the sample. The temperature of this peak is higher compared to the maximum of the first peak of the reduction in  $\text{Co}_3\text{O}_4$ , which can be explained by the higher binding energy of oxygen in the  $\text{MgCo}_2\text{O}_4$  structure.

The behavior of the second TPR peak largely depends on the heat treatment temperature and the Co:Mg ratio in the sample [12,16]. In this work, low-temperature samples containing the spinel phase in the initial state showed a wider second TPR peak than in the case of  $\text{Co}_3\text{O}_4$ , with a maximum at temperatures of 540–620 °C. According to literature studies, with a decrease in the Co content in the catalyst, this peak broadens and shifts to higher temperatures relative to the first peak [16]. In the case of high-temperature samples, which, according to X-ray diffraction data, predominantly contain the solid solution phase in the initial state, the second peak is shifted to the region of 900–1100 °C. This shift occurs sharply between 800 and 900 °C as the calcination temperature increases. In [12], Wang and Ruckenstein argue that the difficulty of  $\text{Co}^{2+}$  reduction in this case is due to the fact that the CoO dispersed in the solid solution lattice contains oxygen, which is also associated with  $\text{Mg}^{2+}$  cations, which are not subject to reduction under these conditions.

It can be assumed that CoO formed following the reduction in  $\text{MgCo}_2\text{O}_4$  spinel during the TPR of low-temperature samples and CoO in the solid solution phase of high-temperature samples are of a different nature. The reduction temperature of CoO according to the literature is 480–500 °C [42], which makes it possible to assert that the second TPR peak of the low-temperature samples relates to the reduction in free CoO, in contrast to the high-temperature samples, where CoO is in a bound state in a solid solution. Therefore, the corresponding phases are of a different nature, although the diffraction patterns obtained after partial reduction to the temperature at which the second peak begins are the same in the case of both Co–Mg(550) and Co–Mg(1100) samples. While this phase is a solid solution in the case of Co–Mg(1100), for the Co–Mg(550) sample, it represents a superposition of two oxides, CoO and MgO, with similar crystal lattices, or a “pseudo” solid solution that turns into a true solid solution at temperatures above 800 °C. The differences between these structures are also due to the size and morphology of their particles. The SEM results showed that the spinel phase and, accordingly, the cubic phase obtained from it during reduction are formed by irregular plate-type particles, while the true solid solution has the form of relatively large bulk crystals with good faceting (Figure 6). The formation of a “pseudo” solid solution during reduction is also supported by the coincidence of the TPR peak region of CoO as an individual compound with the region of the second TPR peak of low-temperature samples, as well as an increase in the reduction temperature when diluting the samples with magnesium oxide.

### 2.3. Catalytic Activity of Samples

The test results of catalyst samples calcined at temperatures of 550, 750, 900, and 1100 °C in the methane combustion reaction are shown in Figure 13. The results of the activity tests of Co–Mg catalysts obtained at a ratio of Co:Mg = 1:1 are also given.

From the data in Figure 13, it follows that the activity of the catalysts decreases with increasing temperature. This is due to the transformation of the spinel phase into the solid solution and the sintering of particles. The activity of the samples obtained with a ratio of Co:Mg = 1:1 differs little from the activity of the samples with a Co:Mg = 2:1 ratio. However, the slope of the curves increases in the vicinity of the 50% degree of conversion. The catalysts synthesized at 550 °C, especially the sample synthesized at a Co:Mg = 1:1

ratio, have the highest activity among the studied samples. The characteristics of the tested catalysts are summarized in Table 6.

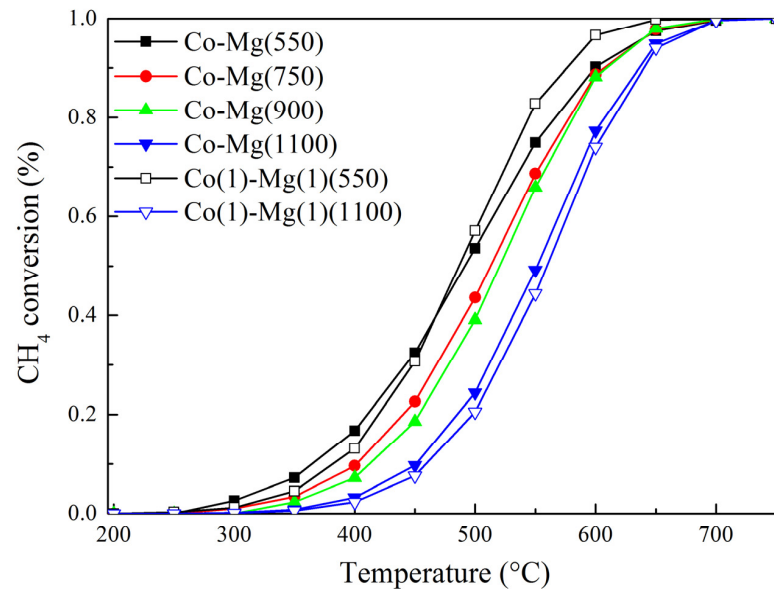


**Figure 13.** Light-off curves of methane conversion over synthesized catalysts.

**Table 6.** Characteristics and activity of synthesized catalysts.

Sample	Specific Area (m <sup>2</sup> /g)	T <sub>50%</sub> (°C)	E (kJ/mol)
Co-Mg(550)	9.6	492	62.1
Co-Mg(750)	7.7	513	74.9
Co-Mg(900)	3.8	521	81.8
Co-Mg(1100)	2.2	551	93.6
Co(1)-Mg(1)(550)	14.9	488	77.6
Co(1)-Mg(1)(1100)	2.8	560	99.2

The resulting relationship between the apparent activation energies calculated from the catalyst test data and the heat treatment temperature at two Co:Mg ratios is presented in Figure 14.

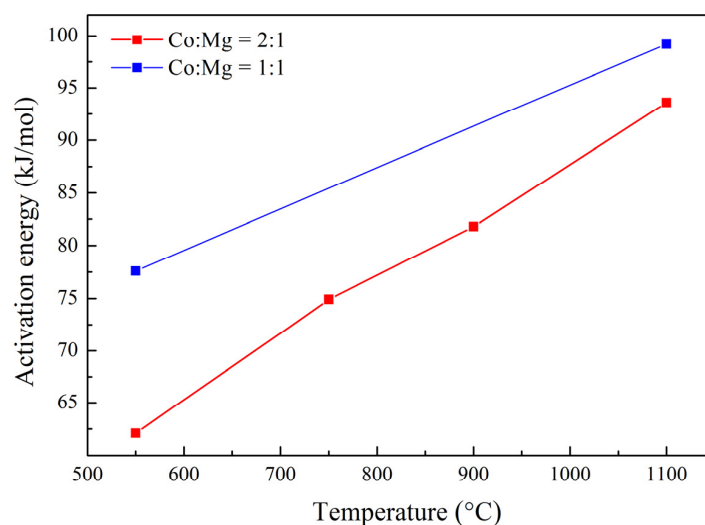


**Figure 14.** Dependence of the apparent activation energy of methane oxidation on the temperature of heat treatment of samples.

From the presented data, it follows that the apparent activation energy of the methane combustion reaction increases linearly with the increasing heat treatment temperature of the catalysts. Moreover, the activation energy values are slightly higher for the Co:Mg = 1:1 ratio. At the same time, the magnitude of the change in the activation barrier upon transition from Co–Mg(550) (spinel) to Co–Mg(1100) (solid solution) is small and amounts to 31.5 kJ/mol, which indicates the similarity of the nature of the active centers on these samples. This is consistent with the data obtained, according to which the repeated formation of spinel structures of the  $\text{Co}_3\text{O}_4$  and/or  $\text{MgCo}_2\text{O}_4$  type occurs during reoxidation on the surface of a solid solution in excess oxygen. Such structures, in particular, are formed during the rapid oxidation and cooling of the samples after heat treatment, as indicated by their TPR profiles (Figure 9), where, even for samples obtained at temperatures above 900 °C, the first peak corresponding to the reduction of  $\text{Co}^{3+}$  to  $\text{Co}^{2+}$  is retained.

The increase in the activation energy of the methane oxidation reaction with increasing heat treatment temperature is logical in the context of the general relationship of these parameters for the Co–Mg oxide system. Figure 15 shows the literature and our data on the activation energies of methane combustion depending on the composition and heat treatment temperature.

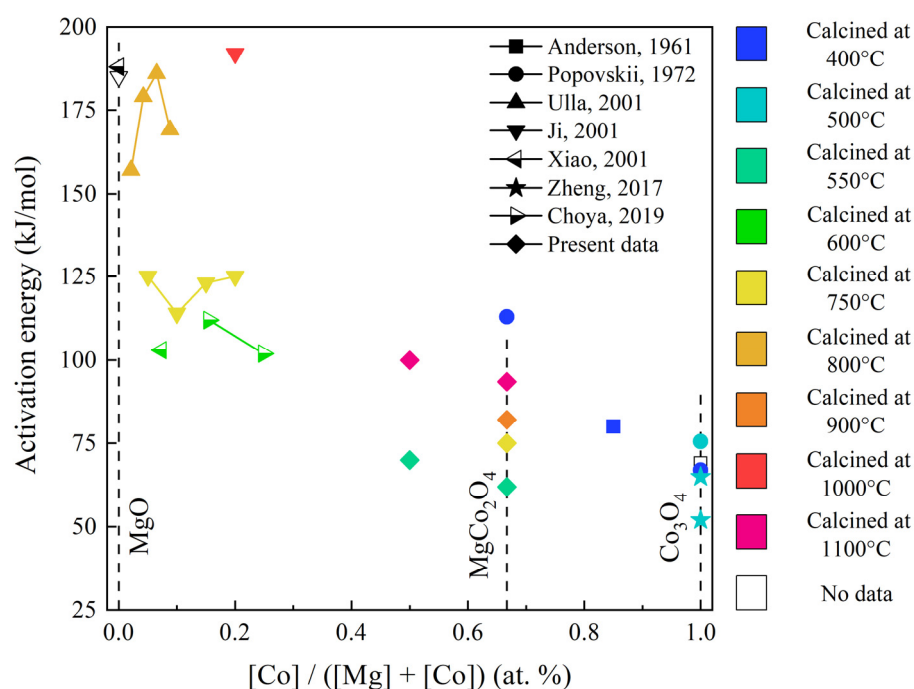


**Figure 15.** Activation energies of methane combustion on Co–Mg catalysts of various compositions and heat treatment temperatures [5,6,10,18–21].

The activation energy for methane combustion on  $\text{Co}_3\text{O}_4$  is low, amounting to 50–70 kJ/mol, and depends on the catalyst preparation technique [5,6,18]. In the case of MgO, the activation energy is much higher and equals 185–190 kJ/mol [20,21].

Intermediate systems, in this regard, can be divided into two categories. Firstly, these are systems with a low cobalt content (Co:Mg < 1:1), where the activation energy of methane oxidation is relatively high (100–180 kJ/mol) [10,19–21] and is characterized by a sharp change with temperature [20]. Secondly, these are systems with a high cobalt content (Co:Mg > 1:1), in which the activation energy is not higher than 100 kJ/mol [5,6,18], with the exception of stoichiometric  $\text{MgCo}_2\text{O}_4$  spinel, obtained and tested by Popovskii and coworkers, for which the value of the activation energy is overestimated due to the inhibition of the reaction by  $\text{CO}_2$  adsorption [6]. The results obtained in this work, presented in Figure 15 along with the literature, are consistent with the general picture of the relationship between these parameters.

### 3. Materials and Methods

#### 3.1. Preparation of Catalysts

Cobalt–magnesium oxide catalysts were synthesized by the thermal decomposition of nitrate salts. The initial mixture of magnesium nitrate ( $\text{Mg}(\text{NO}_3)_2 \cdot 6\text{H}_2\text{O}$ , 99%, Sigma-Aldrich, Darmstadt, Germany) and cobalt ( $\text{Co}(\text{NO}_3)_2 \cdot 6\text{H}_2\text{O}$ ,  $\geq 98\%$ , Sigma-Aldrich, Darmstadt, Germany) powders, taken in a given Co:Mg molar ratio, was dissolved in distilled water. The solution was evaporated on a heated magnetic stirrer with constant stirring. The stirrer was heated with a gradual increase in temperature from 100 to 180 °C for 8 h. The resulting dry product, after removing most of the water from the solution, was transferred to a muffle furnace and calcined at 275 °C for 15 h. The resulting precipitate was thoroughly ground and then calcined at various temperatures. Heat treatment was carried out in a muffle furnace with a heating rate of 10° /min, with samples kept at a given temperature for 1 h. After the end of the heat treatment, the sample was removed from the furnace and rapidly cooled to room temperature. The standard Co:Mg ratio used in this work was 2:1. Samples with this ratio of metals were designated Co–Mg(T), where T is the heat treatment temperature of the sample. Samples with a Co:Mg = 1:1 ratio were designated Co(1)–Mg(1)(T).

Additionally, one of the samples with a Co:Mg = 2:1 ratio was heat treated at 1100 °C for 14 h, after which, in order to study the effect of reoxidation, it was subjected to repeated heat treatment at other, lower, temperatures. The samples obtained in this way were designated Co–Mg(1100 + T), where T is the temperature of the repeated heat treatment of the sample.

Reactive cobalt oxide ( $\text{Co}_3\text{O}_4$ ,  $\geq 98\%$ , Sigma-Aldrich, Darmstadt, Germany) and magnesium oxide obtained from nitrate by heat treatment at 750 °C were also used as standards in the studies.

#### 3.2. Study of Catalysts

The methods of X-ray diffraction (XRD), low-temperature nitrogen adsorption (BET), scanning electron microscopy (SEM), Fourier-transform infrared spectroscopy (FTIR), electron spin resonance (ESR), temperature-programmed desorption of oxygen (TPD), and temperature-programmed reduction by hydrogen ( $\text{H}_2$ -TPR) were used to study the structure of the catalyst samples.

The X-ray diffraction study was carried out on a DRON-4-07 powder diffractometer (Burevestnik, Saint-Petersburg, Russia), Co K $\alpha$  radiation, Ni filter, over a 2 $\theta$  range of 10–90° with a step size of 0.02°. The phase composition analysis according to X-ray diffraction data was carried out on the basis of the areas of diffraction maxima for the spinel and solid solution phases, respectively. The values of the lattice parameters were determined from the positions of the diffraction maxima.

The specific surface area and characteristics of the porous structure of the samples were studied on a Thermo Scientific Surfer gas adsorption porosimeter (Thermo Fisher Scientific, Milan, Italy) at liquid nitrogen temperature using nitrogen ( $\text{N}_2$ ) as an adsorbate. The specific surface area was determined using the Brunauer–Emmett–Teller (BET) method.

The FTIR study was carried out on a Nicolet iS5 FTIR spectrometer (Thermo Fisher Scientific, Milan, Italy) at room temperature in the range of 4000–400  $\text{cm}^{-1}$ . The samples were pressed into KBr pellets.

The structure of the samples was studied by SEM using a low-vacuum scanning electron raster microscope JSM–6610LV (JEOL, Tokyo, Japan) with an attachment for microanalysis and local X-ray fluorescence analysis of the elemental composition of the surface.

The ESR study was carried out on a JES-ME-3X spectrometer (JEOL, Tokyo, Japan), wavelength 3 cm. The spectra were recorded at room temperature. The g-factor values of the samples were determined relative to the DPPH standard.

Temperature-programmed desorption of oxygen (TPD) was carried out using the Khemosorb setup (Novosibirsk, Russia) in a He flow, with a catharometer detector, flow

rate 30 cm<sup>3</sup>/min, heating rate 10 °C/min up to 900 °C. Kinetic analysis of the obtained thermal desorption profiles was carried out using the Polanyi–Wigner equation [51].

Temperature-programmed reduction by hydrogen (H<sub>2</sub>-TPR) was carried out on a self-made installation with analysis of the gas flow on a Chromatek-Kristall 5000 chromatograph (Chromatek, Yoshkar-Ola, Russia) with a catharometer detector. The samples were reduced with a gas mixture of 5% H<sub>2</sub> in Ar. The flow rate was 30 cm<sup>3</sup>/min. Heating was carried out in linear mode at a rate of 10 °C/min to 1100 °C and followed by thermostating at this temperature for 40 min.

The Co–Mg(550) and Co–Mg(1100) samples were studied in detail by TPR with stopping at different temperatures and cooling to room temperature in a flow of H<sub>2</sub>–Ar mixture. The resulting partially reduced samples were studied by XRD and FTIR.

Experiments on methane combustion were carried out in a flow-type setup at atmospheric pressure in a tubular quartz reactor with a fixed bed of catalyst. The catalyst was placed in the central part of the reactor, and quartz wool was located above and below the catalyst layer. The catalytic reaction of methane combustion was carried out at 100–750 °C using a gas mixture of 5% CH<sub>4</sub>, 30% O<sub>2</sub>, and the rest, Ar. The mixture flow rate was 300 mL/min with a catalyst loading volume of 1 cm<sup>3</sup>. An Agilent 6890N gas chromatograph (Agilent Technologies, Singapore Pte. Ltd., Singapore) equipped with a flame ionization detector and a thermal conductivity detector was used to analyze the starting materials and reaction products. The initial gas mixture and reaction products were analyzed on a copper capillary column HP–PLOT Q with a length of 30 m and a diameter of 0.53 mm, filled with polystyrene–divinylbenzene.

The kinetic analysis of the obtained light-off curves of the catalyst samples was carried out at constant gas flow assuming a first-order reaction with respect to methane. The data in the temperature range 100–550 °C was chosen for data fitting in order to avoid the influence of diffusion inhibition [6]. The apparent activation energy for the methane deep oxidation reaction was calculated from the slopes of the corresponding Arrhenius plots using the least squares fitting method. Activation energy values for Co–Mg catalysts of different composition and heat treatment from the literature data were calculated in a similar fashion.

#### 4. Conclusions

A study of Co–Mg catalysts for methane deep oxidation synthesized by the joint thermal decomposition of corresponding nitrate salts was conducted in order to establish formation patterns of the CoO–MgO solid solution from the corresponding stoichiometric spinel and its effect on the catalytic activity. The study confirmed the phase transition of the MgCo<sub>2</sub>O<sub>4</sub> spinel phase to the CoO–MgO solid solution with increasing calcination temperature, primarily above 650 °C. This transformation occurred together with a change in the size and morphology of the catalyst particles. At low calcination temperatures, the catalyst samples also contained small amounts of Co<sup>2+</sup><sub>Td</sub>, presumably corresponding to Co<sub>3</sub>O<sub>4</sub> spinel and decreasing in parallel with the transformation of MgCo<sub>2</sub>O<sub>4</sub> into a solid solution. The release of oxygen from the spinel lattice occurs in the region of this phase transition according to TPD data.

The TPR analysis of the samples calcined at temperatures below the phase transition temperatures confirmed the presence of two peaks of oxygen reduction: the first (420–470 °C) corresponding to the transition of spinel Co<sup>3+</sup><sub>Oh</sub> to Co<sup>2+</sup><sub>Oh</sub> of the rock salt structure, and the second (540–620 °C) to the reduction of Co<sup>2+</sup><sub>Oh</sub> (CoO) to Co<sup>0</sup>. In the case of samples calcined above the phase transition temperature, the first peak decreased significantly, while the second peak moved to the temperature range of 900–1100 °C, presumably corresponding to the reduction of CoO in the true solid solution structure to Co<sup>0</sup>. The XRD analysis of partially reduced samples confirmed the identity of the phases of low-temperature and high-temperature solid solution phases. Despite this, the drastic difference in the reduction temperatures of these phases indicates their fundamental difference: CoO–MgO formed in the low-temperature region during spinel phase reduction is

suggested to be a mixture of ordered oxides that do not form an equilibrium solid solution phase, the formation of which requires higher temperatures (a “pseudo-solid solution”).

Subjecting catalyst samples calcined at 1100 °C to repeated heat treatment at lower temperatures confirmed the ability of the solid solution to partially regenerate through reoxidation. Simultaneously, phase segregation was observed in the regenerated samples, supposedly due to the formation of a new spinel phase enriched in cobalt.

A study of the activity of the synthesized catalysts in the combustion of methane showed high activity of spinel-based samples and a linear correlation of the activation energy of the reaction with the heat treatment temperature. The relatively low change in the activation barrier value during the transition from spinel to a true solid solution indicates the similarity of the nature of their active centers due to the formation of surface spinel even at high heat treatment temperatures upon rapid cooling after calcination.

The results of the study showcase the possibility of obtaining both active and thermally stable Co–Mg deep oxidation catalysts, outlining further prospective studies of the formation patterns of Co–Mg catalysts of other, non-stoichiometric compositions, as well as their activity and long-term regenerative ability in different environments.

**Author Contributions:** Conceptualization, A.S. and I.T.; methodology, B.K. and A.B.; software, K.R.; validation, B.K. and G.X.; formal analysis, M.Z., R.S. and K.R.; investigation, M.Z. and K.K.; resources, Y.A.; data curation, T.B.; writing—original draft preparation, I.T.; writing—review and editing, A.S., A.B. and S.T.; visualization, K.R.; supervision, S.T. and G.X.; project administration, Y.A.; funding acquisition, T.B. All authors have read and agreed to the published version of the manuscript.

**Funding:** This research was funded by the Science Committee of the Ministry of Education and Science of the Republic of Kazakhstan, grant number AP19677006.

**Data Availability Statement:** The data presented in this study are available upon request from the corresponding author.

**Acknowledgments:** The authors are especially grateful to the staff of the Laboratory of Physical and Chemical Research Methods.

**Conflicts of Interest:** The authors declare no conflicts of interest. The funders had no role in the design of the study; in the collection, analyses, or interpretation of data; in the writing of the manuscript; or in the decision to publish the results.

## References

1. Feng, X.; Jiang, L.; Li, D.; Tian, S.; Zhu, X.; Wang, H.; He, C.; Li, K. Progress and key challenges in catalytic combustion of lean methane. *J. Energy Chem.* **2022**, *75*, 173–215. [[CrossRef](#)]
2. Li, K.; Luo, X. Research progress on catalytic combustion of volatile organic compounds in industrial waste gas. *Catalysts* **2023**, *13*, 268. [[CrossRef](#)]
3. Feng, Y.; Liu, Y.; Dai, H.; Deng, J. Review and perspectives of enhancement in the catalytic stability for the complete combustion of CO, CH<sub>4</sub>, and volatile organic compounds. *Energy Fuels* **2023**, *37*, 3590–3604. [[CrossRef](#)]
4. Chen, J.; Arandiyani, H.; Gao, X.; Li, J. Recent advances in catalysts for methane combustion. *Catal. Surv. Asia* **2015**, *19*, 140–171. [[CrossRef](#)]
5. Zheng, Y.; Liu, Y.; Zhou, H.; Huang, W.; Pu, Z. Complete combustion of methane over Co<sub>3</sub>O<sub>4</sub> catalysts: Influence of pH values. *J. Alloys Compd.* **2018**, *734*, 112–120. [[CrossRef](#)]
6. Golodets, G.I. Heterogeneous Catalytic Reactions Involving Molecular Oxygen. *Stud. Surf. Sci. Catal.* **1983**, *15*, 437–469.
7. Choya, A.; de Rivas, B.; Gutiérrez-Ortiz, J.I.; López-Fonseca, R. Comparative study of strategies for enhancing the performance of Co<sub>3</sub>O<sub>4</sub>/Al<sub>2</sub>O<sub>3</sub> catalysts for lean methane combustion. *Catalysts* **2020**, *10*, 757. [[CrossRef](#)]
8. Massenova, A.; Kalykberdiyev, M.; Sass, A.; Kenzin, N.; Ussenov, A.; Baiken, A.; Rakhmetova, K. Catalytic technologies for solving environmental problems in the production of fuels and motor transport in Kazakhstan. *Catalysts* **2020**, *10*, 1197. [[CrossRef](#)]
9. Zhao, L.; Ji, S.; Yin, F.; Lu, Z.; Liu, H.; Li, C. Catalytic combustion of methane over Co<sub>1-x</sub>Mg<sub>x</sub>O/Al<sub>2</sub>O<sub>3</sub>/FeCrAl monolithic catalysts. *J. Nat. Gas Chem.* **2006**, *15*, 287–296. [[CrossRef](#)]
10. Choya, A.; de Rivas, B.; González-Velasco, J.R.; Gutiérrez-Ortiz, J.I.; López-Fonseca, R. On the beneficial effect of MgO promoter on the performance of Co<sub>3</sub>O<sub>4</sub>/Al<sub>2</sub>O<sub>3</sub> catalysts for combustion of dilute methane. *Appl. Catal. A* **2019**, *582*, 117099. [[CrossRef](#)]
11. Chen, L.; Tian, X.; Fu, Y.; Shen, J. The effect of surface acidic and basic properties of highly loaded Co catalysts on the Fischer–Tropsch synthesis. *Catal. Commun.* **2012**, *28*, 155–158. [[CrossRef](#)]

12. Wang, H.Y.; Ruckenstein, E. CO<sub>2</sub> reforming of CH<sub>4</sub> over Co/MgO solid solution catalysts—Effect of calcination temperature and Co loading. *Appl. Catal. A* **2001**, *209*, 207–215. [[CrossRef](#)]
13. Sukri, M.F.F.; Khavarian, M.; Mohamed, A.R. Effect of cobalt loading on suppression of carbon formation in carbon dioxide reforming of methane over Co/MgO catalyst. *Res. Chem. Intermed.* **2018**, *44*, 2585–2605. [[CrossRef](#)]
14. El-Salamony, R.A.; Morshedy, A.S.; El Naggat, A.M.A. Elevated CO-free hydrogen productivity through ethanol steam reforming using cubic Co-nanoparticles based MgO catalyst. *Environ. Technol.* **2022**, *43*, 1860–1869. [[CrossRef](#)]
15. Furusawa, T.; Tsutsumi, A. Development of cobalt catalysts for the steam reforming of naphthalene as a model compound of tar derived from biomass gasification. *Appl. Catal. A* **2005**, *278*, 195–205. [[CrossRef](#)]
16. Wang, H.Y.; Ruckenstein, E. Partial oxidation of methane to synthesis gas over alkaline earth metal oxide supported cobalt catalysts. *J. Catal.* **2001**, *199*, 309–317. [[CrossRef](#)]
17. Moral, A.; Reyero, I.; Llorca, J.; Bimbela, F.; Gandía, L.M. Partial oxidation of methane to syngas using Co/Mg and Co/Mg-Al oxide supported catalysts. *Catal. Today* **2019**, *333*, 259–267. [[CrossRef](#)]
18. Anderson, R.B.; Stein, K.C.; Feenan, J.J.; Hofer, L.J.E. Catalytic oxidation of methane. *Ind. Eng. Chem.* **1961**, *53*, 809–812. [[CrossRef](#)]
19. Ulla, M.A.; Spretz, R.; Lombardo, E.; Daniell, W.; Knözinger, H. Catalytic combustion of methane on Co/MgO: Characterisation of active cobalt sites. *Appl. Catal. B* **2001**, *29*, 217–229. [[CrossRef](#)]
20. Ji, S.-F.; Xiao, T.-C.; Wang, H.-T.; Flahaut, E.; Coleman, K.S.; Green, M.L.H. Catalytic combustion of methane over cobalt-magnesium oxide solid solution catalysts. *Catal. Lett.* **2001**, *75*, 65–71. [[CrossRef](#)]
21. Xiao, T.-C.; Ji, S.-F.; Wang, H.-T.; Coleman, K.S.; Green, M.L. Methane combustion over supported cobalt catalysts. *J. Mol. Catal. A Chem.* **2001**, *175*, 111–123. [[CrossRef](#)]
22. Kiselev, V.F.; Krylov, O.V.B. *Adsorption and Catalysis on Transition Metals and Their Oxides*; Springer: Berlin/Heidelberg, Germany, 1989; p. 445.
23. Robin, J. Recherches sur la constitution et la stabilité de quelques solutions solides a base d'oxyde de cobalt. *Ann. Chim.* **1955**, *12*, 389–412.
24. Zamudio, M.A.; Bensaid, S.; Fino, D.; Russo, N. Influence of the MgCo<sub>2</sub>O<sub>4</sub> preparation method on N<sub>2</sub>O catalytic decomposition. *Ind. Eng. Chem. Res.* **2011**, *50*, 2622–2627. [[CrossRef](#)]
25. Fadlalla, M.I.; Nyathi, T.M.; Claeys, M. Magnesium as a methanation suppressor for iron- and cobalt-based oxide catalysts during the preferential oxidation of carbon monoxide. *Catalysts* **2022**, *12*, 118. [[CrossRef](#)]
26. Zigla, A.A.; Kox, T.; Mevoa, D.; Assaouka, H.T.; Nsangou, I.N.; Daawe, D.M.; Kenmoe, S.; Kouotou, P.M. Magnesium-modified Co<sub>3</sub>O<sub>4</sub> catalyst with remarkable performance for toluene low temperature deep oxidation. *Catalysts* **2022**, *12*, 411. [[CrossRef](#)]
27. Veselov, G.B.; Stoyanovskii, V.O.; Cherepanova, S.V.; Vedyagin, A.A. Sol-gel prepared Co-Mg-O oxide systems: Redox behavior, thermal stability and catalytic performance in CO oxidation. *React. Kinet. Mech. Catal.* **2023**, *136*, 233–250. [[CrossRef](#)]
28. Ya, M.; Wang, J.; Li, G.; Gao, G.; Zhao, X.; Cui, J.; Wu, H.; Li, L. Surface engineering in MgCo<sub>2</sub>O<sub>4</sub> spinel oxide for an improved oxygen evolution reaction. *ACS Sustain. Chem. Eng.* **2023**, *11*, 744–750. [[CrossRef](#)]
29. Han, X.; Wang, L.; Ling, H.; Ge, Z.; Lin, X.; Dai, X.; Chen, H. Critical review of thermochemical energy storage systems based on cobalt, manganese, and copper oxides. *Renew. Sustain. Energy Rev.* **2022**, *158*, 112076. [[CrossRef](#)]
30. Wang, H.; Mi, N.; Sun, S.; Zhang, W.; Yao, S. Oxygen vacancies enhancing capacitance of MgCo<sub>2</sub>O<sub>4</sub> for high performance asymmetric supercapacitors. *J. Alloys Compd.* **2021**, *869*, 159294. [[CrossRef](#)]
31. Kamioka, N.; Ichitsubo, T.; Uda, T.; Imashuku, S.; Taninouchi, Y.K.; Matsubara, E. Synthesis of spinel-type magnesium cobalt oxide and its electrical conductivity. *Mater. Trans.* **2008**, *49*, 824–828. [[CrossRef](#)]
32. Hagan, A.P.; Lofthouse, M.G.; Stone, F.S.; Trevethan, M.A. High surface area oxide solid solution catalyst. *Stud. Surf. Sci. Catal.* **1979**, *3*, 417–438.
33. Holgersson, S.; Karlsson, A. Röntgenographische Untersuchungen einiger Mischkristallsysteme mit Monoxyden als Komponenten. *Z. Anorg. Allg. Chem.* **1929**, *182*, 255–271. [[CrossRef](#)]
34. Krezhov, K.; Konstantinov, P. On the cationic distribution in Mg<sub>x</sub>Co<sub>3-x</sub>O<sub>4</sub> spinels. *J. Phys. Condens. Matter* **1992**, *4*, L543–L548. [[CrossRef](#)]
35. Casas-Cabanas, M.; Binotto, G.; Larcher, D.; Lecup, A.; Giordani, V.; Tarascon, J.M. Defect chemistry and catalytic activity of nanosized Co<sub>3</sub>O<sub>4</sub>. *Chem. Mater.* **2009**, *21*, 1939–1947. [[CrossRef](#)]
36. McCormack, S.J.; Navrotsky, A. Thermodynamics of high entropy oxides. *Acta Mater.* **2021**, *202*, 1–21. [[CrossRef](#)]
37. Ichimura, H.; Komatsu, W. Distribution of various dopants cations (Li<sup>+</sup>, Al<sup>3+</sup>, Ga<sup>3+</sup>, and In<sup>3+</sup>) in cobalt spinel. *J. Chem. Soc. Jpn.* **1972**, *4*, 690–695.
38. Peshev, P.; Toshev, A.; Gyurov, G. Preparation of high-dispersity MCo<sub>2</sub>O<sub>4</sub> (M = Mg, Ni, Zn) spinels by thermal dissociation of coprecipitated oxalates. *Mater. Res. Bull.* **1989**, *24*, 33–40. [[CrossRef](#)]
39. Yagi, S.; Ichikawa, Y.; Yamada, I.; Doi, T.; Ichitsubo, T.; Matsubara, E. Synthesis of binary magnesium-transition metal oxides via inverse co-precipitation. *Jap. J. Appl. Phys.* **2013**, *52*, 025501. [[CrossRef](#)]
40. Syeda, A.F.; Khan, M.N. Spin state of cobalt and electrical transport in MgCo<sub>2</sub>O<sub>4</sub> system. *J. Supercond. Nov. Magn.* **2018**, *31*, 3545–3551. [[CrossRef](#)]
41. Aukrust, E.; Muan, A. Activities of components in oxide solid solutions: The systems CoO–MgO, CoO–MnO, and CoO–FeO at 1200 °C. *Trans. Metall. Soc. AIME* **1963**, *227*, 1378–1380.

42. Wang, C.W.; Wang, C.B.; Chien, S.H. Characterization of cobalt oxides studied by FT-IR, Raman, TPR and TG-MS. *Thermochim. Acta* **2008**, *473*, 68–73.
43. Nayak, S.; Dasari, K.; Joshi, D.C. Spectroscopic studies of  $\text{Co}_2\text{TiO}_4$  and  $\text{Co}_3\text{O}_4$  two-phase composites. *Phys. Status Solidi B* **2016**, *253*, 2270–2282. [[CrossRef](#)]
44. Dyrek, K.; Sojka, Z. Coordination and dispersion of  $\text{Co}^{2+}$  ions in  $\text{CoO-MgO}$  solid solutions. *J. Chem. Soc. Faraday Trans. 1 Phys. Chem. Condens. Phases* **1982**, *78*, 3177–3185. [[CrossRef](#)]
45. Gazzoli, D.; Occhiuzzi, M.; Cimino, A.; Cordischi, D.; Minelli, G.; Pinzari, F. XPS and EPR study of high and low surface area  $\text{CoO-MgO}$  solid solutions: Surface composition and  $\text{Co}^{2+}$  ion dispersion. *J. Chem. Soc. Faraday Trans.* **1996**, *92*, 4567–4574. [[CrossRef](#)]
46. Querini, C.A.; Ulla, M.A.; Requejo, F.; Soria, J.; Sedrán, U.A.; Miró, E.E. Catalytic combustion of diesel soot particles. Activity and characterization of  $\text{Co/MgO}$  and  $\text{Co, K/MgO}$  catalysts. *Appl. Catal. B* **1998**, *15*, 5–19. [[CrossRef](#)]
47. Dutta, P.; Seehra, M.S.; Thota, S.; Kumar, J. A comparative study of the magnetic properties of bulk and nanocrystalline  $\text{Co}_3\text{O}_4$ . *J. Phys. Condens. Matter* **2008**, *20*, 015218. [[CrossRef](#)]
48. Gardner, T.J.; Messing, G.L. Magnesium salt decomposition and morphological development during evaporative decomposition of solutions. *Thermochim. Acta* **1984**, *78*, 17–27. [[CrossRef](#)]
49. Raveau, B.; Seikh, M. *Cobalt Oxides: From Crystal Chemistry to Physics*; Wiley-VCH: Weinheim, Germany, 2012; p. 333.
50. Guan, D.; Shi, C.; Xu, H.; Gu, Y.; Zhong, J.; Sha, Y.; Hu, Z.; Ni, M.; Shao, Z. Simultaneously mastering operando strain and reconstruction effects via phase-segregation strategy for enhanced oxygen-evolving electrocatalysis. *J. Energy Chem.* **2023**, *82*, 572–580. [[CrossRef](#)]
51. De Jong, A.M.; Niemantsverdriet, J.W. Thermal desorption analysis: Comparative test of ten commonly applied procedures. *Surf. Sci.* **1990**, *233*, 355–365. [[CrossRef](#)]

**Disclaimer/Publisher’s Note:** The statements, opinions and data contained in all publications are solely those of the individual author(s) and contributor(s) and not of MDPI and/or the editor(s). MDPI and/or the editor(s) disclaim responsibility for any injury to people or property resulting from any ideas, methods, instructions or products referred to in the content.